Current Optics and Photonics
Vol. 3, No. 3, June 2019, pp. 227-235

ISSN: 2508-7266(Print) / ISSN: 2508-7274(Online)
DOI: https://doi.org/10.3807/COPP.2019.3.3.227

# Design and Experimental Demonstration of Coaxially Folded All-reflective Imaging System

**Yupeng Xiong[1,2,3], Yifan Dai[1,2,3]*, Shanyong Chen[1,2,3], and Guipeng Tie[1,2,3]**

[1]*College of Intelligent Science, National University of Defense Technology, Changsha 410073, China*
[2]*Laboratory of Science and Technology on Integrated Logistics Support, National University of Defense Technology, Changsha 410073, China*
[3]*Hu'nan Key Laboratory of Ultra-precision Machining Technology, Changsha 410073, China*

(Received November 29, 2018 : revised April 10, 2019 : accepted April 11, 2019)

With slimmer, lighter and all-reflective imaging systems in high demand for consumer and military applications, coaxially folded optical image systems are widely considered because they can extend focal length and reduce track length. Most of these systems consist of multiple surfaces, and these surfaces are machined on one element or grouping processing on two elements. In this paper, we report and first experimentally demonstrate an all-aluminum all-reflective optical system which consists of two optical elements, with two high order aspherical surfaces in each element. The coaxially folded system is designed with Seidel aberration theory and advanced optimization with Zemax. The system is made of all-aluminum material processing by single point diamond turning (SPDT). On this basis, we completed the system integration and performed an imaging experiment. The final system has the advantages of short track length and long focal length and broad application prospects in the micro-unmanned aerial vehicle field.

*Keywords* : Optical design, Coaxially folded imaging system, Tolerance analysis, Optical manufacture, Imaging experiment
*OCIS codes* : (110.0110) Imaging systems; (220.0220) Optical design and fabrication; (220.1250) Aspherics

## I. INTRODUCTION

Nowadays, with the deep development of optoelectronic imaging technology in the field of unmanned aerial vehicle systems and image identification, coaxially folded all-reflective system has become a new hot point. It has achromatic and athermal aberrations, can allow wide spectral range, has a large aperture, is lightweight and small in volume, and has great merits in heat tolerance. Most of these systems included aspherical and freeform surfaces and are increasingly attracting the attention of researchers, so some valuable efforts have been done made on the development of the coaxially folded optical system. Tremblay [1-3] conducted multiple researches on coaxial folded optical systems based on calcium fluoride materials under the support of the Defense Advanced Research Projects Agency (DARPA). And it was successfully applied to the human eye assisted imaging system [4]. But all the systems inevitably introduce chromatic aberration. Zhang [5, 6] and Ge [7] also put into practice related research work of simulation and can provide reference for optical design, but the process is not described in detail and did not report the performance of the actual system. Li [8] report an ultrathin zoom telescopic objective consisting of an annular folded lens and three electro-wetting liquid lenses, but the design process is not described in detail.

In this paper, we report and first experimentally demonstrate an all-aluminum all-reflective optical system which consists of two optical elements with two high order aspherical surfaces in each element, the field of view (FOV) is 1°. The coaxially folded system is designed with Seidel aberration theory. The design results show that the

*Corresponding author: dyf@nudt.edu.com, ORCID 0000-0002-0220-6315
Color versions of one or more of the figures in this paper are available online.

imaging quality of the system reaches the diffraction limit. And the system is made of all-aluminum material processing by single point diamond turning (SPDT). On this basis, the integration and imaging experiment is realized.

## II. OPTICAL DESIGN PROCEDURE

### 2.1. Initial Structure and Optimization

The layout of the coaxially four-mirror optical system is shown in Fig. 1. As the light from the outermost annular aperture enters the optical system and then reflects back and forth through the "Z" shape between the front and back surfaces and then reaches the detector. A longer focal length can be achieved within a limited thickness. The axial compression of the optical system can be achieved to a compact structure. $M_1$, $M_3$ and $M_2$, $M_4$ can be processing in one optical element.

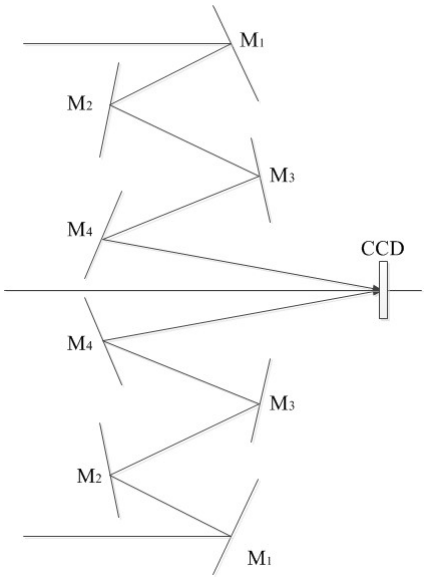


FIG. 1. Layout of coaxially folded system.

For the coaxially folded four mirror optical system, the starting point of optical design can be gotten from the conventional four mirror system, the structure is shown in Fig. 2. $M_1$, $M_2$, $M_3$ and $M_4$ represent primary mirror, secondary mirror, tertiary mirror and quaternary mirror, the optical stop is on the primary mirror. The physical meaning of the specific parameters is as follows: $h_i$ represents the projected height of the first paraxial ray on each surface, $d_i$ means the distance from the current mirror to the next mirror, F is the focus point of the system and the total focal length of the system is $f'$. The conic coefficients employed in the structure of each mirror are $e_1^2$, $e_2^2$, $e_3^2$, $e_4^2$ the obscuration ratios of $M_1$, $M_2$ and $M_3$ are $\alpha_1 \approx h_2/h_1$, $\alpha_2 \approx h_3/h_2$, $\alpha_3 \approx h_4/h_3$. respectively, and the magnifications of $M_2$, $M_3$ and $M_4$ are $\beta_2 \approx (l_2')/l_2$, $\beta_3 \approx (l_3')/l_3$, $\beta_4 \approx (l_4')/l_4$, respectively. The image quality for the four-mirror system is decided by choosing the structure parameters $\alpha_1$, $\alpha_2$, $\alpha_3$, $\beta_2$, $\beta_3$, and $\beta_4$.

According to the third-order aberration theory and to previous design experience [9-11], we can get the third-order aberration of three reflective system in Eq. (1).

$$
\begin{aligned}
S_I &= \sum hP + \sum h^4 K = A_1 + \sum h^4 K \\
S_{II} &= \sum yP - J\sum W + \sum h^3 yK = A_2 + \sum h^3 yK \\
S_{III} &= \sum \frac{y^2}{h} P - 2J\sum \frac{y}{h} W + J^2 \sum \phi \\
&\quad + \sum h^2 y^2 K = A_3 + \sum h^2 y^2 K \\
S_{IV} &= \sum \frac{\Pi}{h} \\
S_V &= \sum \frac{y^3}{h^2} P - 3J\sum \frac{y^2 W}{h^2} + J^2 \sum \frac{y}{h}\left(3\phi + \frac{\Pi}{h}\right) - J^3 \\
&\quad \sum \frac{1}{h^2}\Delta\left(\frac{1}{n^2}\right) + \sum hy^3 K = A_4 + \sum hy^3 K
\end{aligned}
\tag{1}
$$

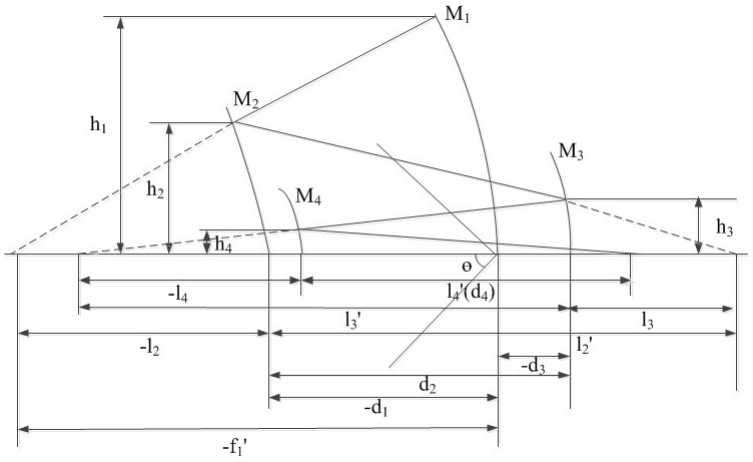


FIG. 2. Structure of concentric multi-reflective optic.

In Eq. (1), parameters of $P$, $W$, $\Pi$, $K$, $J$, can be calculated as $P=\left(\frac{\Delta u}{\Delta\left(\frac{1}{n}\right)}\right)^2\Delta\left(\frac{u}{n}\right)$, $W=\frac{\Delta u}{\Delta\left(\frac{1}{n}\right)}\Delta\left(\frac{u}{n}\right)$, $\Pi=\frac{\Delta(nu)}{nn'}$, $\phi=\frac{1}{h}\Delta\left(\frac{u}{n}\right)$, $K=-\frac{e^2}{R^3}\Delta(n)$, $J=1$. Here $u$ is the angle between the incident light and the optical axis. We can get Eq. (2) with the system structure parameters $r$, $d$.

$$\alpha_1=1-\frac{2d_1}{r_1},\ \beta_1=-\frac{r_2}{r_2-r_1+2d_1}$$

$$\alpha_2=1-\frac{2d_2(r_1\_2d_1-r_2)}{r_2(r_1-d_1)},\ \beta_2=\frac{r_3}{\beta_1 r_1-2\beta_1 d_1-2d_2-r_3}$$

$$\alpha_3=1-\frac{2d_3}{\alpha_1\alpha_2\beta_1\beta_2 r_1},\ \beta_3=\frac{2f}{\beta_2\beta_1 r_1} \tag{2}$$

For a four-reflection system, the refractive index of the object space and image space of each mirror are $n_1=n_2'=n_3=n_4'=1$ and $n_1'=n_2=n_3'=n_4=-1$. For the paraxial ray, we can get the initial conditions $h_1=1$, $f'=1$, $\theta=-1$ We can get $h_1=1$, $h_2=\alpha_1$, $h_3=\alpha_1\alpha_2$, $h_4=\alpha_1\alpha_2\alpha_3$, $u_1=0$, $u_1'=u_2=\beta_1\beta_2\beta_3$, $u_2'=u_3=\beta_2\beta_3$, $u_3'=u_4=\beta_3$, $u_4'=1$, $\triangle(u)_1=\beta_1\beta_2\beta_3$, $\triangle(u)_2=(1-\beta_1)\beta_2\beta_3$, $\triangle(u)_3=(1-\beta_2)\beta_3$, $\triangle(u)_4=1-\beta_3$, $\triangle(nu)_1=-\beta_1\beta_2\beta_3$, $\triangle(nu)_2=(1+\beta_1)\beta_2\beta_3$, $\triangle(nu)_3=-(1+\beta_2)\beta_3$, $\triangle(nu)_4=1+\beta_3$, $\triangle\left(\frac{u}{n}\right)_1=-\beta_1\beta_2\beta_3$, $\triangle\left(\frac{u}{n}\right)_2=(1+\beta_1)\beta_2\beta_3$, $\triangle\left(\frac{u}{n}\right)_3=-(1+\beta_2)\beta_3$, $\triangle\left(\frac{u}{n}\right)_4=1+\beta_3$, $\triangle\left(\frac{1}{n}\right)_1=-2$, $\triangle\left(\frac{1}{n}\right)_2=2$, $\triangle\left(\frac{1}{n}\right)_3=-2$, $\triangle\left(\frac{1}{n}\right)_4=2$, $n_1n_1'=n_2n_2'=n_3n_3'=n_4n_4'=1$ and Eq. (3).

$$y_1=0,\ y_2=\frac{\alpha_1-1}{\beta_1\beta_2\beta_3}$$

$$y_3=\frac{\alpha_2(\alpha_1-1)+\beta_1(1-\alpha_2)}{\beta_1\beta_2\beta_3} \tag{3}$$

$$y_4=\frac{\alpha_3\alpha_2(\alpha_1-1)+\alpha_3\beta_1(1-\alpha_2)+\beta_1\beta_2(\alpha_3-1)}{\beta_1\beta_2\beta_3}$$

Normalized aspheric coefficient $K_i$ are shown in Eq. (4).

$$K_1=\frac{e_1^2}{4}\beta_1^2\beta_2^2\beta_3^2,\ K_2=-\frac{e_1^2}{4}\frac{(1+\beta_1)^3\beta_2^2\beta_3^2}{\alpha_1^3}$$

$$K_3=\frac{e_3^2}{4}\frac{(1+\beta_2)^3\beta_3^2}{\alpha_1^3\alpha_2^3},\ K_4=\frac{e_3^2}{4}\frac{(1+\beta_3)^3}{\alpha_1^3\alpha_2^3\alpha_3^3} \tag{4}$$

As the radius of curvature of the four mirrors meets the condition of the flat field in Eq. (5).

$$\frac{1}{R_1}-\frac{1}{R_2}+\frac{1}{R_3}-\frac{1}{R_4}=0 \tag{5}$$

Spherical coefficients $P_i$ and coma coefficients $W_i$ of each mirror are shown in Eq. (6).

$$P_1=-\frac{\beta_1^3\beta_2^3\beta_3^3}{4},\ W_1=\frac{\beta_1^2\beta_2^2\beta_3^2}{2},\ \Pi_1=\beta_1\beta_2\beta_3,\ \phi_1=-\beta_1\beta_2\beta_3$$

$$P_2=\frac{\beta_2^3\beta_3^3(1+\beta_1)(1-\beta_1)^2}{4},\ W_2=\frac{\beta_3^2\beta_2^2(1+\beta_1)(1-\beta_1)}{2},$$
$$\Pi_2=-(1+\beta_1)\beta_2\beta_3,\ \phi_2=\frac{(1+\beta_1)\beta_2\beta_3}{\alpha_1}$$

$$P_3=-\frac{\beta_3^3(1-\beta_2)^2(1+\beta_2)}{4},\ W_3=\frac{\beta_3^2(1+\beta_2)(1-\beta_2)}{2},$$
$$\Pi_3=(1+\beta_2)\beta_3,\ \phi_3=\frac{-(1+\beta_2)\beta_3}{\alpha_1\alpha_2}$$

$$P_4=-\frac{(1-\beta_3)^2(1+\beta_3)}{4},\ W_4=\frac{(1+\beta_3)(1-\beta_3)}{2},$$
$$\Pi_4=-(1+\beta_3),\ \phi_4=\frac{1+\beta_3}{\alpha_1\alpha_2\alpha_3} \tag{6}$$

In order to achieve the purpose of eliminating the monochromatic aberrations, we can suppose $S_I=S_{II}=S_{III}=S_V=0=(S_{II})$, we can get the following linear Eq. (7). In Eq. (7), $h_i$, $y_i$ and $A_i$ can be calculated from the equations above.

$$\begin{bmatrix} h_1^4 & h_2^4 & h_3^4 & h_4^4 \\ h_1^3y & h_2^3y & h_3^3y & h_2^3y \\ h_1^2y^2 & h_2^2y^2 & h_3^2y^2 & h_4^2y^2 \\ h_1y^3 & h_2y^3 & h_3y^3 & h_4y^3 \end{bmatrix}\begin{bmatrix} K_1 \\ K_2 \\ K_3 \\ K_4 \end{bmatrix}=-\begin{bmatrix} A_1 \\ A_2 \\ A_3 \\ A_4 \end{bmatrix} \tag{7}$$

According to the overall requirements of the system, the specifications of the folded imaging system are shown in Table 1, the working wavelength is 0.45~0.75 μm, the field of view (FOV) is 0.1, the $d_{out}$ is 30 mm and $d_{in}$ is 20 mm, the total focal length is 30 mm, the total axial length of the system is within 10 mm, the imaging element is the 1/2-inch CMOS MT9M001C12STM, the pixel size is 5.2 μm and the number is 1280 × 1024.

For the coaxially folded system, we assume that the four surfaces are all a quadric surface, which is represented by the Eq. (8)., where $c$ represents the curvature (the reciprocal of the radius), r is the radial coordinate in lens unit and $k$ is the conic constant.

$$z=\frac{cr^2}{1+\sqrt{1-(1+k)c^2r^2}} \tag{8}$$

TABLE 1. Specifications of folded imaging system

| Parameters | Values |
|---|---|
| Wavelength/μm | 0.45~0.75 |
| FOV/° | 1 |
| $d_{out}$/mm | 30 |
| $d_{in}$/mm | 20 |
| Focal length/ mm | 30 |
| Total axial length l/ mm | <10 |
| Pixel number | 1280 × 1024 |
| Pixel size/μm | 5.2 |

In order to make the system more compact, we can get the initial conditions $d_1 \approx d_2 \approx d_3 \approx d_4$. According to the above theory and method, we can get the initial parameters of the system which is shown in Table 2, $M_1$, $M_2$, $M_3$ and $M_4$ are all hyperboloid with Zemax, we obtain the optical performance, the layout is shown in Fig. 3(a), the MTF is in Fig. 3(b), the spot radius is in Fig. 3(c) and the field curvature and distortion are in Fig. 3(d).

Then we change the surface type in Zemax from standard surface to even aspheric surface and add 12-th order coefficients. The even aspheric surface sag is given by Eq. (9).

TABLE 2. Initial parameters of four mirror folded system

| Surface | Radius | Thickness |
|---|---|---|
| $M_1$ | -43.576 | -4.850 |
| $M_2$ | 229.697 | 4.700 |
| $M_3$ | 107.812 | -4.895 |
| $M_4$ | -27.388 | - |

$$z = \frac{cr^2}{1+\sqrt{1-(1+k)c^2r^2}} + \alpha_1 r^2 + \alpha_2 r^4 + \alpha_3 r^6 + \alpha_4 r^8 + \alpha_5 r^{10} + \alpha_6 r^{12} \quad (9)$$

where $c$ represents the curvature, $k$ is the conic constant, $\alpha_i (i = 1, 2, \cdots 8)$ is the coefficients of aspheric surface and $r$ is the radial coordinate to describe the aspheric surface. We further optimize system performance by setting multiple variables and the optimal results are shown in Fig. 4. By contrasting Fig. 4(b) with the Fig. 3(b), we could find the MTF obviously increasing, and the values in all fields are approximately at the diffraction limit. The root-mean-square (RMS) radiuses are also decreased by several times after the optimization. The distortion decreases 100 times after the optimization and the value is smaller than 0.005%. And the RMS value of wavefront aberration

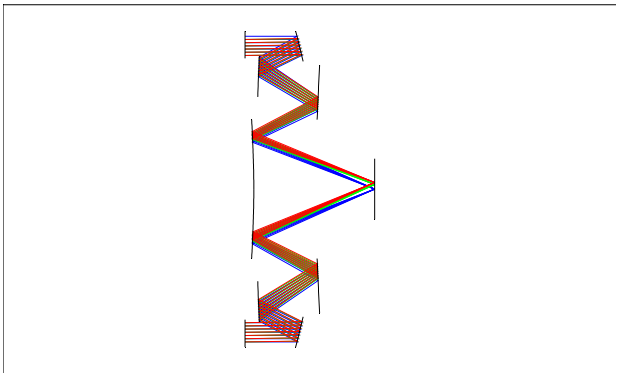

(a) The initial layout

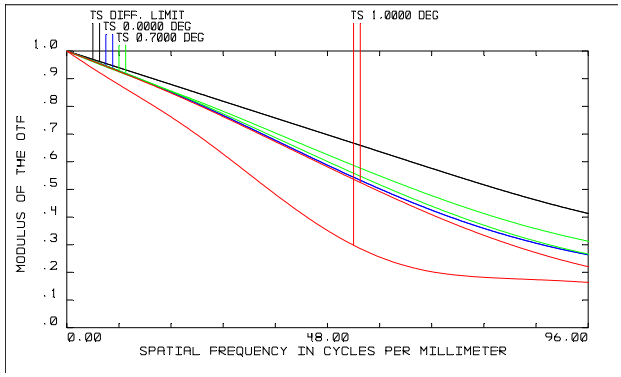


(b) The initial MTF

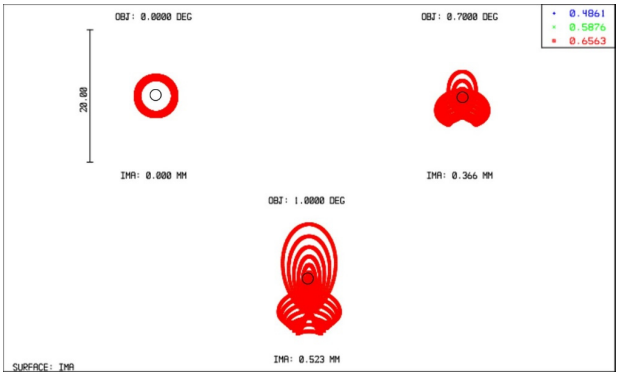


(c) The initial spot radius

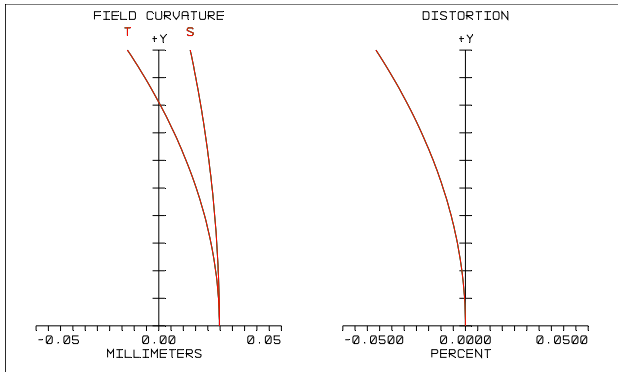


(d) The field curvature and distortion

FIG. 3. The initial design results.

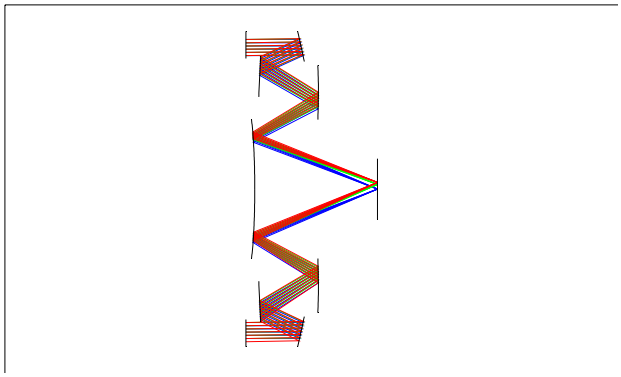

(a) The optimal layout

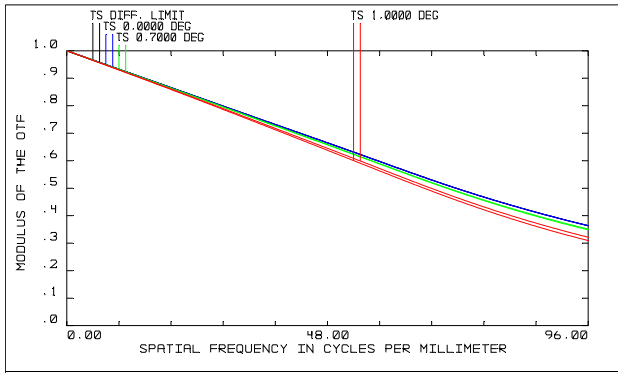


(b) The optimal MTF

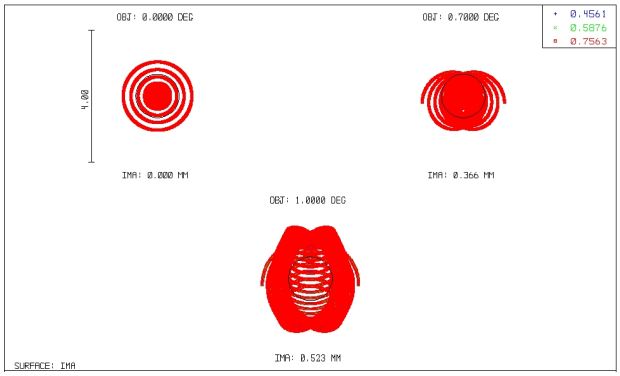


(c) The optimal spot radius

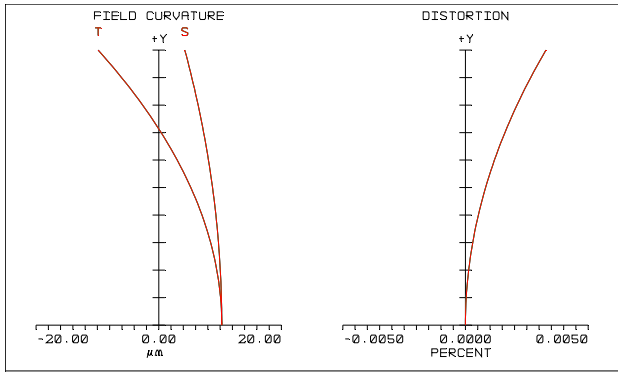


(d) The optimal field curvature and distortion

FIG. 4. The optimal design results.

TABLE 3. Results of tolerances analysis

| Description | | Tolerance value | RMS spot radius change |
|---|---|---|---|
| Thickness | **$M_1$-$M_2$** | **-2 μm** | **0.621 μm** |
| | | **+2 μm** | **0.626 μm** |
| | $M_2$-$M_3$ | -2 μm | 0.288 μm |
| | | +2 μm | 0.288 μm |
| | $M_3$-$M_4$ | -2 μm | 0.288 μm |
| | | +2 μm | 0.283 μm |
| Surface tilt (x,y) | $M_1$ | ±0.05° | 0.044 μm |
| | **$M_2$** | **±0.05°** | **0.186 μm** |
| | $M_3$ | ±0.05° | 0.101 μm |
| | $M_4$ | ±0.05° | 0.034 μm |
| Surface decenter (x,y) | $M_1$ | ±4 μm | 0.112 μm |
| | $M_2$ | ±4 μm | 0.00008 μm |
| | **$M_3$** | **±4 μm** | **0.140 μm** |
| | $M_4$ | ±4 μm | 0.0002 μm |
| Radius | **$M_1$** | **-12 μm** | **0.937 μm** |
| | | **+12 μm** | **0.926 μm** |
| | $M_2$ | -12 μm | 0.0004 μm |
| | | +12 μm | 0.0004 μm |
| | $M_3$ | -12 μm | 0.112 μm |
| | | +12 μm | 0.112 μm |
| | $M_4$ | -12 μm | 0.00004 μm |
| | | +12 μm | 0.00004 μm |

is 0.0062 λ (λ = 0.6328 μm). For an ideal imaging system, according to the Marechal criterion, the RMS value of wavefront error must be smaller than 1/14 λ.

### 2.2. Tolerance Analysis

The coaxially folded optical system is assembled by two monolithic multi-surface optical elements on one single substrate, so the tolerances for the system are tighter by reason of more constraints. The tolerances are given in Table 3 under testing wavelength 632.8 nm. The most sensitive type of tolerance is displayed in bold. For the coaxially folded system, the nominal fabrication tolerances are determined from a sensitivity analysis and the back focal length is the compensator. The criterion is defined as the size of the RMS spot radius smaller than one pixel. According to the results, the thickness tolerances of aspherical surfaces are ±2 μm and the most sensitive one is the thickness between $M_1$ and $M_2$. The surface tilt tolerances are ±0.05° and the most sensitive surface is $M_2$. The surface decenter tolerances are ±4 μm and the most sensitive surface is $M_3$. The radius tolerances are ±12 μm and the most sensitive surface is $M_1$. The nominal RMS spot radius is 2.844 μm and the estimated change 1.787 μm, so the estimated RMS spot radius is 4.631 μm which is smaller than one pixel size 5.2 μm. And the range of focus compensation required for the visible system is from -11.27 μm to +11.27 μm under these tolerances. For this folded system, once the optical elements are processed and formed, the position between the optical elements cannot be adjusted. The shape and position accuracy can only be guaranteed by the machining accuracy. Even if the shape and position of each optical element are machined in place, there may be eccentricity and tilt between the two rings of aspherical surfaces. So manufacture and measurement are important for quality control. And taking into account tolerances and the poor accuracy of the printed-circuit board (PCB) of the CCD, an adjustable screw displacement mechanism is designed between the CCD and the optical elements. The stroke of the displacement mechanism is ±2 mm, and the pitch of the micro-motion thread is 0.5 mm.

## III. MANUFACTURE AND EXPERIMENT

### 3.1. Optical Manufacture

As we all know, the accuracy of surface figure and surface relative position directly affect the performance of the system, and according to the layout of the coaxially fold imaging system shown in Fig. 1, high order aspheric mirrors $M_1$, $M_3$ and $M_2$, $M_4$ are together processed in one optical element which reduces both the centration errors in fabrication and alignment errors in assembly. The single-point diamond turning technology (SPDT) is a mature method for manufacturing aspheric mirrors and free-form optics with submicron precision. The optical material used for the system is aluminum alloy (Al6061). Through the reasonable preparation of a multi-ring aspheric surface machining program, the use of a 180° arc diamond tool (tool radius R = 1 mm), and the tool radius compensation are used to realize the processing of the aspheric multi-surfaces. In order to meet the tolerance requirements, the removal of each characteristic dimension of the optics is under the order of sub-micron scale. The ultra-precision machining results are shown in Fig. 5. Figure 5(a) is the processing and physical map of the element-I with $M_2$ and $M_4$, both $M_2$ and $M_4$ are convex surfaces and the annular zone between $M_2$ and $M_4$ is painted black to suppress the stray light in some degree. Figure 5(b) is the processing and physical map of the element-II with $M_1$ and $M_3$, both $M_1$ and $M_3$ are concave surfaces.

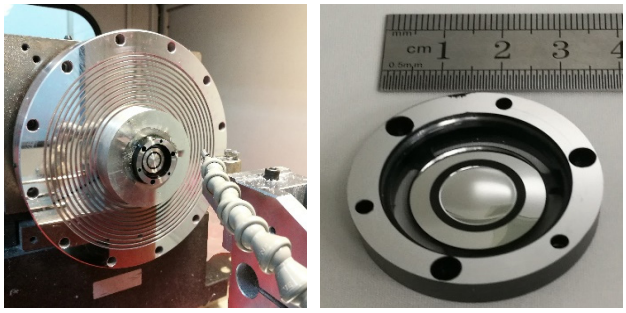

(a) Element-I with $M_2$ and $M_4$

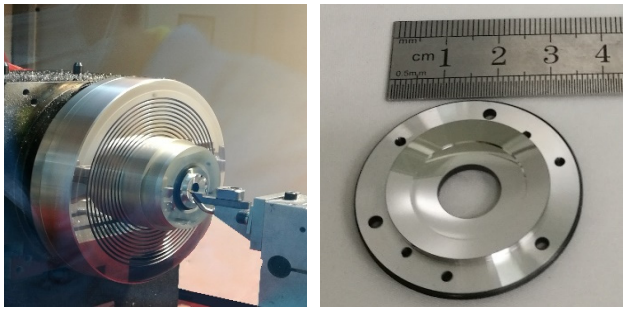

(b) Element-II with $M_1$ and $M_3$

FIG. 5. Fabrication of optical surfaces.

### 3.2. Integration and Performance Analysis

The wavefront error of system comes from two aspects, one is the surface error which contains surface figure error and surface position error, the other is the assembled error including eccentricity and tilt error between the two elements and the mirror deformation caused by the assembly stress. According to our previous measurement results, the peak and valley value (PV) of all surface is within 0.56 λ (λ = 0.6328 μm) and the RMS value is 0.99 λ, and the position accuracy is smaller than 0.15 λ, all the values above are within the demand of the tolerances. And because the aspherical annular surfaces on the same optical element is smaller in size, the MRF (magnetorheological finishing) and CMP (chemical mechanical polishing) methods which can further improve the accuracy of the surfaces are difficult

to work, so the surface shape and positional accuracy after processing are difficult to improve.

The matching surface between element-I and element-II is a high-precision plane which is machined by SPDT (the black surface) and the system is fixed by three screws on the edge which are shown in Fig. 6. So the tilt error between the two elements is very small. Consequently, the system assembly error mainly comes from eccentricity of element-I and element-II. According to Zemax simulation results, the RMS wavefront errors caused by decenter of 1 micron in the x or y direction is 0.0004 λ (RMS), the biggest error tolerance for the decenter is about 50 μm. So

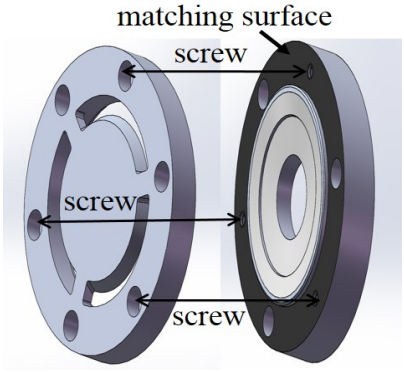


FIG. 6. Assembly screws and matching surface of system.

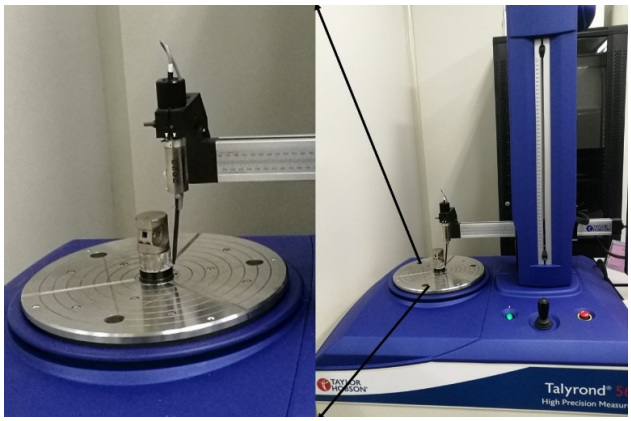


(a) Assembly with Talyrond 565H

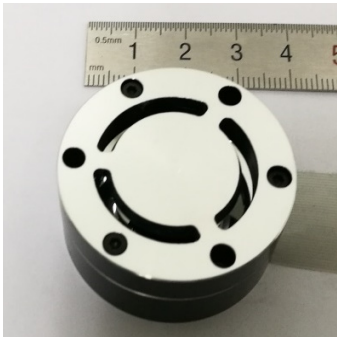

(b) Assembly result

FIG. 7. Decenter control with Talyrond 565H.

we attempt to control the coaxial error with the help of Talyrond 565H and the control experiment is shown in Fig. 7(a). We first fixed the element-II on the roundness meter platform with hot melt adhesive, then measured the roundness of the element-II and calculated the position of the center position of the circle $C_1$, then fitted the element-I onto the component 2, we add a weight on the top of the system in order to increase the stability of the system, then we measure the roundness, calculate the position of the center position of the circle $C_2$, and the difference of $D = C_1 - C_2$ represents the decenter of the two elements. When the value of D is smallest we fixed the system with 502 glue and then tightened with the assembly screws. The best result we obtained is about 97 microns, and the finally assemble result is shown in Fig. 7(b).

After the integration of the system, we analyzed the optical performance by testing the wavefront. The wavefront testing experimental system is in Fig. 8(a). The laser beam of 632.8 nm emitted from the Zygo interferometer passes through a flat mirror and enters into the folded system,

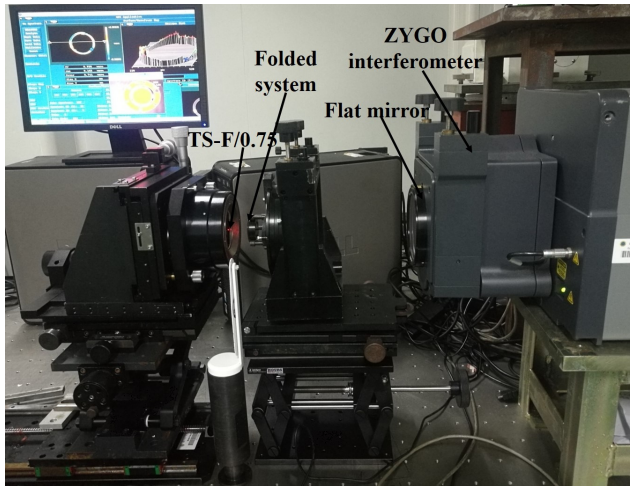


(a) The experimental system of wavefront

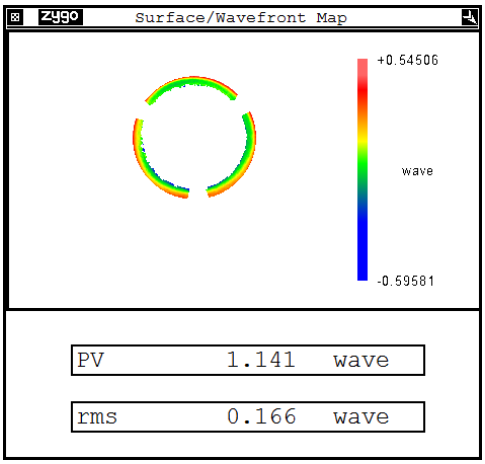


(b) Wavefront result

FIG. 8. Wavefront of the system.

after coinciding with the focus of the imaging system, then the light reflects back along the original path to form interference fringes by a transmission sphere (TS) of F/0.75. The results are shown in Fig. 8(b), the PV value of the wavefront aberration is 1.414 λ and the RMS value of the wavefront aberration is 0.166 λ. For the system, the residual RMS wavefront aberration of the design is 0.0062 λ, and the wavefront aberration caused by the decenter of two optical elements is 0.0388λ, and the other wavefront aberrations all come from the surface figure error and the surface deformation caused by the torque of the assembly screw. And the system performance can be improved by further improving the surface quality and assembly method.

The imaging experiments are carried out to detect the US Air Force (USAF) 1951 resolution detection card which is shown in Fig. 9.

The details of the experiment are shown in Fig. 10, the USAF 1951 chart is placing 5.4 m far away from the folded imaging system. And the left is the experimental diagram, the right is the imaging result. According to the imaging result, the system can resolve the sixth strip of the negative one group, so the resolution is approximately 0.891 lp/mm.

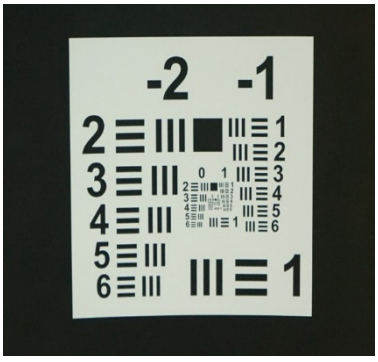


FIG. 9. The USAF 1951 chart.

## IV. CONCLUSION

From the viewpoint of application, physical configuration of an optical system is important. In this paper, we report and first experimentally demonstrate a coaxially folded optical system which consists of two optical elements, and there are two high order aspherical surfaces in each element. This is an all-reflective system which is designed with Seidel aberration theory and the procedure to obtain the original structural parameters is studied. The system is made of all-aluminum material processing by single point diamond turning (SPDT) and the system is assembled with the help of a roundness meter in order to control the decenter degree of two optical elements. In addition, the wavefronts are measured by a wavefront interference me thod. On this basis, we performed an imaging experiment to detect the USAF 1951 chart at the distance of 5.4 m, and the resolution is about 0.891 lp/mm. There is room for further improvement in image quality, and it is necessary to improve the shape and position accuracy by the means of compensation machining and to improve assembly.

## ACKNOWLEDGMENT

This research was supported by the National Nature Science Foundation of China (NSFC) No. 51835013, and the authors thank Dr. Zhanbin Fan for valuable discussions.

## REFERENCES

1. E. J. Tremblay, J. Rutkowski, I. Tamayo, P. E. X. Silveira, R. A. Stack, R. L. Morrison, M. A. Neifeld, Y. Fainman, and J. E. Ford, "Relaxing the alignment and fabrication tolerances of thin annular folded imaging systems using wavefront coding," Appl. Opt. **46**, 6571-6578 (2007).

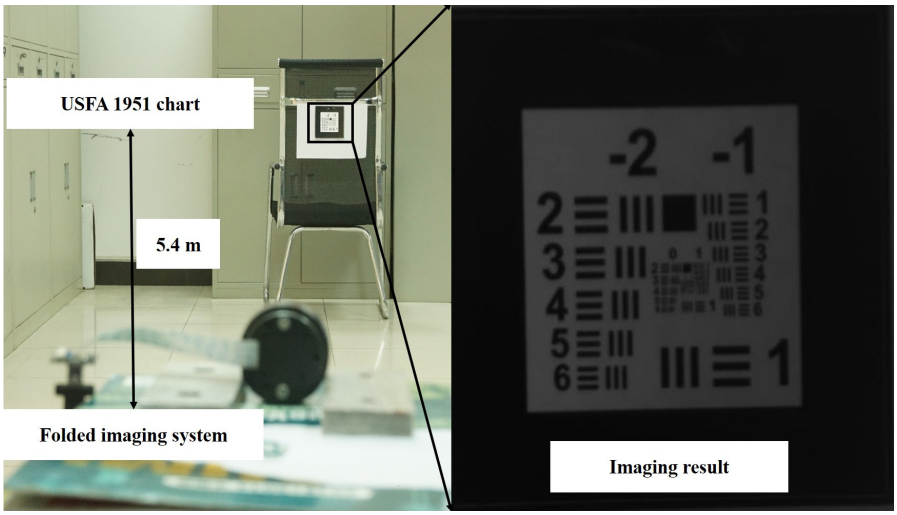


FIG. 10. Imaging results of system.

2. E. J. Tremblay, R. A. Stack, R. L. Morrison, and J. E. Ford, "Ultrathin cameras using annular folded optics," Appl. Opt. **46**, 463-471 (2007).
3. E. J. Tremblay, R. A. Stack, R. L. Morrison, and J. E. Ford, "Annular folded optic imager," Proc. SPIE **6232**, 62320R (2006).
4. A. Ashkan, M. S. Glenn, E. J. Tremblay, I. Stamenov, A. Groisman, J. Legerton, W. Meyers, G. A. Amigo, and J. E. Ford, "Wearable telescopic contact lens," Appl. Opt. **54**, 7195-7205 (2015).
5. R. Zhang and W. Shen, "Ultrathin lenses using annular folded optics," Infrared Laser Eng. **41**, 1306-1311 (2012).
6. R. Zhang and W. Shen, "Ultrathin lenses using annular folded optics," Proc. SPIE **7156**, 715604 (2008).
7. L. Ge and Z. Liang, "Micro-optics label receiving system based on annular aperture ultra-thin lens," Acta Opt. Sin. **35**, 1222001-1-222001-6 (2015).
8. L. Li and D. Wang, "Ultrathin zoom telescopic objective," Opt. Express **24**, 18674-18685 (2016).
9. J. U. Lee and S. M. Yu, "Analytic design procedure of three-mirror telescope corrected for spherical aberration, comma, astigmatism and Petzval field curvature," J. Opt. Soc. Korea **13**, 184-192 (2009).
10. X. L. Li, M. Xu, X. D. Ren, and Y. T. Pei, "An optical design of off-axis four-mirror-anastigmatic telescope for remote sensing," J. Opt. Soc. Korea **16**, 243-246 (2012).
11. M. F. Zou, J. Chang, M. M. Talha, T. C. Zhang, and Y. T. Wang, "Design and analysis of the four-mirror optical system," Optik **121**, 1900-1903 (2010).